

## ON MULTIFRACTIONALITY OF SPHERICAL RANDOM FIELDS WITH COSMOLOGICAL APPLICATIONS

PHILIP BROADBRIDGE<sup>1</sup>, RAVINDI NANAYAKKARA<sup>1</sup> and ANDRIY OLENKO<sup>1</sup>

(Received 20 August, 2021; accepted 2 June, 2022; first published online 18 August, 2022)

### Abstract

This paper investigates spatial data on the unit sphere. Traditionally, isotropic Gaussian random fields are considered as the underlying mathematical model of the cosmic microwave background (CMB) data. We discuss the generalized multifractional Brownian motion and its pointwise Hölder exponent on the sphere. The multifractional approach is used to investigate the CMB data from the Planck mission. These data consist of CMB radiation measurements at narrow angles of the sky sphere. The results obtained suggest that the estimated Hölder exponents for different CMB regions do change from location to location. Therefore, the CMB temperature intensities are multifractional. The methodology developed is used to suggest two approaches for detecting regions with anomalies in the cleaned CMB maps.

2020 *Mathematics subject classification*: primary 60G60; secondary 60G15, 60G22, 62M40, 83F05, 62P35.

*Keywords and phrases*: random fields, multifractionality, Hölder exponent, spherical statistics, cosmic microwave background radiation, CMB anomalies.

### 1. Introduction

The notion of fractional Brownian motion (FBM) was introduced by Mandelbrot and Van Ness in 1968 [31]. The Hurst parameter  $H$  can be used to define the Hölder regularity of the FBM [7]. The multifractional Brownian motion (MBM) was first considered by Péltier and Lévy Véhel in 1995, extending the FBM [38]. The concept of multifractionality allows local fractional properties to depend on space-time locations. Multifractional processes were used to study complex stochastic systems which exhibit nonlinear behaviour in space and time. Multifractional behaviour of data has been found in many applications, such as image processing, stock price movements and signal processing [7, 41].

<sup>1</sup>Department of Mathematics and Statistics, La Trobe University, Melbourne, VIC 3086, Australia; e-mail: P.Broadbridge@latrobe.edu.au, D.Nanayakkara@latrobe.edu.au, A.Olenko@latrobe.edu.au  
© The Author(s), 2022. Published by Cambridge University Press on behalf of Australian Mathematical Publishing Association Inc. This is an Open Access article, distributed under the terms of the Creative Commons Attribution licence (<https://creativecommons.org/licenses/by/4.0/>), which permits unrestricted re-use, distribution, and reproduction in any medium, provided the original work is properly cited.

The generalized multifractional Brownian motion (GMBM) is a continuous Gaussian process that was introduced by generalizing the traditional FBM and MBM (see [7]). In comparison to MBM, the Hölder regularity of GMBM can vary substantially. For example, GMBM can allow discontinuous Hölder exponents. This has been an advantage in certain applications, such as medical image modelling, telecommunications, turbulence and finance, where the pointwise Hölder exponent can change rapidly. A Fourier spectrum's low frequencies control the long-range dependence of a stochastic process while the higher frequencies control the Hölder regularity. Therefore, GMBM can be used to model processes that exhibit erratic behaviour of the local Hölder exponent and long-range dependence [7].

The aim of this paper is to introduce new applied methodology based on the local Hölder exponent, and illustrate it by applying it to cosmic microwave background (CMB) radiation data. The following brief physics background is provided to enable a better understanding of the CMB data.

The universe originated about 14 billion years ago and was characterized by an extremely high temperature. The cosmological theory that is generally accepted is given, for example, in the book by Weinberg [45]. From  $10^{-35}$  seconds (s) after the original singularity up to  $10^{-32}$  s, there was rapid exponential inflation by a factor greater than  $e^{60}$ , driven by an as yet unidentified inflation quantum field. Correlation lengths following from vacuum energy fluctuations rapidly expanded to separations that are now observed in the CMB to be well beyond the horizon of light signals. Inflation is an answer to the horizon puzzle as well as the flatness puzzle and the absence of magnetic monopoles. From  $10^{-5}$  s after the singularity, hadron particle–antiparticle pairs could form, followed by lepton pairs from 1 s. By 10 s, the universe had cooled enough so that pair annihilation led to photons being the dominant component of energy within the plasma for the next 380,000 years. During this time, within the plasma, the photon mean free path was relatively short, so the system was opaque. However, from 100,000 years onwards, He atoms and then neutral H atoms began to form. In the final stage of “recombination”, at temperature almost 4000 kelvin (K), after 378,000 years the photons propagated freely and can be observed in the CMB. Due to cosmological expansion, their wavelengths have now stretched to the microwave part of the electromagnetic spectrum, exhibiting a high-accuracy blackbody spectrum of a thermalized environment, matching with a temperature of 2.725 K. However, small anisotropic perturbations of that temperature are now of most interest. They indicate large-scale density variations within the plasma universe that are associated with preferred locations in the subsequent formation of galaxies. Further back, anisotropy relates to the formation of matter, separating rival quantum field theories.

On a sphere, a scalar function such as temperature is most conveniently expanded in a basis of spherical harmonics in polar coordinates  $Y_l^m(\theta, \varphi)$ . The largest variation from isotropy is a dipole structure at  $l = 1$ . That dipole can be transformed away by choosing a reference frame that has a speed of 368 km/s relative to our own frame. There is significant structure in the spherical harmonic spectrum up to at least  $l = 1000$ .

There is a consistent interpretation that we are now in a dark-energy-dominated era, consisting of 73% or more of the mass energy, around 23% dark matter, the small but important remainder being ordinary matter and radiation.

In the microwave region, the CMB spectrum closely follows that of a black body at equilibrium temperature 2.735 K, tracing back to a plasma temperature of around 4000 K at a time corresponding to redshift  $z = 1500$  at 50% atomic combination. Although the equilibrium spectrum is essential, there are important departures from equilibrium that give information on the state of the early universe. Relative anisotropic variations of spectral intensity from that of a black body are of the order of  $10^{-4}$ . Calculations by Khatri and Sunyaev [25] showed that outside of a relatively small range of redshifts, external energy inputs from sources such as massive particle decay would dissipate by Compton and double Compton scattering and other relaxation processes to affect the signal by several lower orders of magnitude. The primary sources of anisotropy were large-scale acoustic waves whose compressions in the plasma universe were associated with raised temperatures. Using the current angular widths of anisotropies in the CMB, the current standard model  $\Lambda$ CDM (cold dark matter plus dark energy) affords an estimate of the Hubble constant at  $H_0 = 67.4 \pm 1.4$  km/s/Mpc [4]. This agrees well with data from the POLARBEAR Antarctica telescope that give  $H_0 = 67.2 \pm 0.57$  km/s/Mpc [2]. However, estimates from more recent emissions from closer galaxies, using both cepheid variables and type Ia supernovae as distance markers, give  $H_0 = 74.03 \pm 1.42$  km/s/Mpc [40]. This unexplained discrepancy will eventually be resolved by newly found errors in the methodology of one or both of the competing large- $z$  and small- $z$  measurements, or in new physical processes that are currently unidentified.

Within a turbulent plasma, there are electro-dynamical processes that are far more complicated than the large-scale acoustic waves. When radiation by plasma waves is taken into account, useful kinetic equations and spectral functions can no longer be constructed by Bogoliubov's approach of closing the moment equations for electron distribution functions (see [26, Ch. 5]). Even in controlled tokamak devices, the dynamical description of magnetic field lines has fractal attracting sets [43], and charged particle trajectories may have fractal attractors under the influence of multiple magnetic drift waves [34]. At CMB frequencies below 3 GHz (that is, wavelengths larger than 10 cm), there have been indications of spectral intensities much higher than that of a 2.7 K black body [8]. Although there is a high level of confidence in measuring the universe's expansion factor from the CMB since the decoupling of photons from charged particles, the level of complexity of magnetohydrodynamics in plasma suggests that this subject might not be a closed book. Multifractal analysis is a tool that might contribute to understanding the multiscale data that are becoming successively finer-grained with each generation of radio telescope.

The Planck mission [39] was launched in 2009 to measure the CMB with an extraordinary accuracy over a wide spectrum of infrared wavelengths. The signal obtained has been filtered by astrophysics teams using the best available technology. We feel that it is worthwhile to analyse the full signal that is currently available. Higher-resolution

measurements in the future will distinguish which details of the analysis are due to physical causes, or various sources of galactic noise and measurement errors. Either way, a retrospective correction of our analysis could guide future signal processing.

The CMB data can be utilized to understand how the early universe originated and to find out the key parameters of the Big Bang model [37]. Numerous researchers have suggested that the CMB data either are non-Gaussian or cannot be accurately described by mathematical models with few constant parameters (see [3, 29, 32, 36]). The classical book by Weinberg [45] explained that this anisotropy in the plasma universe was significant enough to produce anisotropy in current galaxy distributions. For some recent results and discussion of fundamental cosmological models of the universe see [12]. To detect departures from the isotropic model in actual CMB data several approaches can be employed (see, for example, [21, 29]). Different approaches can give different results, and suggest to cosmologists sky regions for further investigations. The motivation of this paper is to check for multifractionality of the CMB temperature intensities from the Planck mission. Theoretical multifractional space-time models which differ from the standard cosmological model [15] have suggested that the universe is not expanding monotonically, which produces multifractional behaviour. Calcagni et al. [15] used the CMB data from the Planck mission and the Far Infrared Absolute Spectrophotometer to establish speculative constraints on multifractional space-time expansion scenarios. Further, fractional stochastic partial differential equations (SPDEs) were employed to model the CMB data [5]. The fractional SPDE models considered exhibited long-range dependence.

In the literature, the most widely used model for describing CMB temperature intensities is isotropic Gaussian spherical random fields (see, for example, [3, 27, 33] for more details). Mathematical analysis of spherical random fields has attracted significant research attention in recent years (see [21, 28, 33] and the references therein). This paper continues these investigations. It develops methodology to investigate fractional properties of random fields on the unit sphere. The presented detailed analysis of actual CMB temperature intensities suggests the presence of multifractionality.

The methodology developed was also used to detect anomalies in CMB maps. The results obtained were compared with a different method from [21]. Both methods found the same anomalies, but each detected its own CMB regions of unusual behaviour. Applications of the methodology developed resulted in spatial clusters that matched very well with the temperature confidence mask (TMASK) of unreliable CMB intensities.

Developing a methodology to detect multifractional behaviour and anomalies within the random fields framework is quite natural. In the CMB research context, determining areas with unusual Hölder exponent values can indicate locations of seeds of galaxies or areas that are problematic for preliminary signal processing of CMB maps. The anomalous locations detected are regions of potential interest for further investigations by astronomers, in particular, using analytic tools that are not yet routinely used.

The structure of the paper is as follows. Section 2 provides the main notation and definitions related to the theory of random fields. Section 3 introduces the concept of multifractality and discusses the GMBM. Section 4 presents results on the estimation of the pointwise Hölder exponent by using quadratic variations of random fields. Section 5 discusses the suggested estimation methodology. Numerical studies including computing the estimates of pointwise Hölder exponents for different one- and two-dimensional regions of the CMB sky sphere are given in Section 6. This section also demonstrates an application of our methodology to detect regions with anomalies in the cleaned CMB maps. Finally, the conclusions and some future research directions are presented in Section 7.

All numerical studies were carried out by using Python version 3.9.4 and R version 4.0.3, specifically, the R package RCOSMO [18, 19]. A reproducible version of the code in this paper is available in the “Research materials” folder at the website <https://sites.google.com/site/olenkoandriy/>.

## 2. Main notation and definitions

This section presents background material in the theory of random fields, fractional spherical fields and fractional processes. Most of the material included in this section is based on the papers [6, 27, 30, 33].

Let  $\mathbb{R}^3$  be the real three-dimensional Euclidean space and  $s_2(1)$  be the unit sphere defined in  $\mathbb{R}^3$ . That is,  $s_2(1) = \{x \in \mathbb{R}^3, \|x\| = 1\}$  where  $\|\cdot\|$  represents the Euclidean distance in  $\mathbb{R}^3$ . Let  $SO(3)$  denote the group of rotations on  $\mathbb{R}^3$ .

Let  $(\Omega, \mathcal{F}, P)$  be a probability space. The symbol  $\stackrel{d}{=}$  denotes equality in the sense of the finite-dimensional distributions.

**DEFINITION 2.1.** A function  $T(\omega, x) : \Omega \times s_2(1) \rightarrow \mathbb{R}$  is called a real-valued random field defined on the unit sphere. For simplicity, it will also be denoted by  $T(x)$ ,  $x \in s_2(1)$ .

**DEFINITION 2.2.** The random field  $T(x)$  is called strongly isotropic if, for all  $k \in \mathbb{N}$ ,  $x_1, \dots, x_k \in s_2(1)$  and  $g \in SO(3)$ , the joint distributions of the random variables  $T(x_1), \dots, T(x_k)$  and  $T(gx_1), \dots, T(gx_k)$  have the same law.

It is called 2-weakly isotropic (in the following it will be just called isotropic) if the second moment of  $T(x)$  is finite, that is, if  $E(|T(x)|^2) < \infty$  for all  $x \in s_2(1)$  and if for all pairs of points  $x_1, x_2 \in s_2(1)$ , and for any rotation,  $g \in SO(3)$ , we have

$$E(T(x)) = E(T(gx)), \quad E(T(x_1)T(x_2)) = E(T(gx_1)T(gx_2)).$$

**DEFINITION 2.3.** The random field  $T(x)$  is called Gaussian if for all  $k \in \mathbb{N}$  and  $x_1, \dots, x_k \in s_2(1)$  the random variables  $T(x_1), \dots, T(x_k)$  are multivariate Gaussian distributed, that is,  $\sum_{i=1}^k a_i T(x_i)$  is a normally distributed random variable for all  $a_i \in \mathbb{R}$ ,  $i = 1, \dots, k$ , such that  $\sum_{i=1}^k a_i^2 \neq 0$ .

Let  $T = \{T(r, \theta, \varphi) \mid 0 \leq \theta \leq \pi, 0 \leq \varphi < 2\pi, r > 0\}$  be a spherical random field that has zero mean, finite variance and is mean-square continuous. Let the corresponding

Lebesgue measure on the unit sphere be  $\sigma_1(du) = \sigma_1(d\theta \cdot d\varphi) = \sin \theta \, d\theta \, d\varphi$ , with  $u = (\theta, \varphi) \in s_2(1)$ . For two points on  $s_2(1)$ , we use  $\Theta$  to denote the angle formed between two rays originating at the origin and pointing at these two points, and  $\Theta$  is called the *angular distance* between these two points. To emphasize that a random field depends on Euclidean coordinates, the notation  $\tilde{T}(x) = T(r, \theta, \varphi)$ ,  $x \in \mathbb{R}^3$ , will be used.

**REMARK 2.4.** In the following, for analysis of cosmological data, we will also be using the galactic coordinate system with the Sun as the centre to locate the relative positions of objects and motions within the Milky Way. This consists of galactic longitude  $l$ ,  $0 \leq l < 2\pi$ , and galactic latitude  $b$ ,  $-\pi/2 \leq b \leq \pi/2$ . They are related to the spherical coordinates by  $l = \phi$  and  $b = (\pi/2 - \theta)$ .

**REMARK 2.5.** A real-valued second-order random field  $\tilde{T}(x)$ ,  $x \in s_2(1)$ , with  $E(\tilde{T}(x)) = 0$  is isotropic if  $E(\tilde{T}(x_1)\tilde{T}(x_2)) = B(\cos \Theta)$ ,  $x_1, x_2 \in s_2(1)$ , depends only on the angular distance  $\Theta$  between  $x_1$  and  $x_2$ .

The spherical harmonics are defined by

$$Y_l^m(\theta, \varphi) = c_l^m \exp(im\varphi)P_l^m(\cos \theta), \quad l = 0, 1, \dots; \quad m = 0, \pm 1, \dots, \pm l,$$

with

$$c_l^m = (-1)^m \left( \frac{2l+1}{4\pi} \frac{(l-m)!}{(l+m)!} \right)^{1/2},$$

and the Legendre polynomials  $P_l^m(\cos \theta)$  having degree  $l$  and order  $m$ .

Then the following spectral representation of spherical random fields holds in the mean-square sense:

$$T(r, \theta, \varphi) = \sum_{l=0}^{\infty} \sum_{m=-l}^l Y_l^m(\theta, \varphi) a_l^m(r),$$

where  $a_l^m(r)$  is a set of random coefficients defined by

$$a_l^m(r) = \int_0^\pi \int_0^{2\pi} T(r, \theta, \varphi) \overline{Y_l^m(\theta, \varphi)} r^2 \sin \theta \, d\theta \, d\varphi = \int_{s_2(1)} \tilde{T}(ru) \overline{Y_l^m(u)} \sigma_1(du),$$

with  $u = x/||x|| \in s_2(1)$ ,  $r = ||x||$ .

**DEFINITION 2.6.** A real-valued random field  $\tilde{T}(x)$ ,  $x \in \mathbb{R}^3$ , has stationary increments, if the equality

$$\tilde{T}(x+x') - \tilde{T}(x') \stackrel{d}{=} \tilde{T}(x) - \tilde{T}(0), \quad x \in \mathbb{R}^3,$$

holds for all  $x' \in \mathbb{R}^3$ .

**REMARK 2.7.** When  $\tilde{T}(x)$ ,  $x \in \mathbb{R}^3$ , is a second-order random field with stationary increments, then one has  $E(\tilde{T}(x+x') - \tilde{T}(x'))^2 = \mathcal{V}_{\tilde{T}}(x)$  for every  $(x, x') \in \mathbb{R}^3 \times \mathbb{R}^3$ , where  $\mathcal{V}_{\tilde{T}}$  is called the *variogram* of the field  $\tilde{T}$ .

**DEFINITION 2.8.** A real-valued random field  $\tilde{T}(x)$ ,  $x \in \mathbb{R}^3$ , is said to be globally self-similar if, for some fixed positive real number  $H$  and for each positive real number  $a$ , it satisfies

$$a^{-H}\tilde{T}(ax) \stackrel{d}{=} \tilde{T}(x), \quad x \in \mathbb{R}^3. \quad (2.1)$$

**REMARK 2.9.** Beside the degenerate case, the scale invariance property (2.1) holds only for a unique  $H$  which we declare as the global self-similarity exponent.

**DEFINITION 2.10.** For each fixed  $H \in (0, 1)$ , there exists a real-valued globally  $H$ -self-similar isotropic centred Gaussian field with stationary increments. This is called the *fractional Brownian field* (FBF) of Hurst parameter  $H$ , and is denoted by  $B_H(t)$ ,  $t \in \mathbb{R}^3$ . The corresponding covariance function, is given, for all  $(t', t'') \in \mathbb{R}^3 \times \mathbb{R}^3$ , by

$$E(B_H(t')B_H(t'')) = 2^{-1} \text{Var}(B_H(\mathbf{e}_0))(\|t'\|^{2H} + \|t''\|^{2H} - \|t' - t''\|^{2H}),$$

where  $\mathbf{e}_0$  denotes an arbitrary vector of the unit sphere  $s_2(1)$ .

**REMARK 2.11.** In the particular case where  $H = 1/2$ , the FBF is denoted by  $B(t)$ ,  $t \in \mathbb{R}^3$ , and is called *Lévy Brownian motion*.

Similarly, one can introduce an  $H$ -self-similar process in the one-dimensional case. We also denote it by  $B_H(t)$ ,  $t \geq 0$ . It will be called the *fractional Brownian motion* (FBM).

**DEFINITION 2.12 [38].** The FBM with Hurst parameter  $H(0 < H < 1)$  is defined by the stochastic integral

$$B_H(t) = \frac{1}{\Gamma(H + 1/2)} \left\{ \int_{-\infty}^0 ((t-s)^{H-1/2} - (-s)^{H-1/2}) dW(s) + \int_0^t (t-s)^{H-1/2} dW(s) \right\},$$

where  $t \geq 0$  and  $W(\cdot)$  denotes a Wiener process on  $(-\infty, \infty)$ .

The Hurst parameter specifies the degree of self-similarity. When  $H = 0.5$ , the FBM reduces to the standard Brownian motion. In contrast to the Brownian motion, the increments of FBM are correlated.

### 3. Multifractional processes

This section provides definitions and theorems related to multifractional processes. Most of the material presented in this section is based on [6, 9, 10, 38].

Let  $C^1$  be the class of continuously differentiable functions and  $C^2$  be the class of functions where both first and second derivatives exist and are continuous.

First, we introduce multifractional processes in the one-dimensional case. These will be used to analyse the CMB temperature intensities using the ring ordering Hierarchical Equal Area isoLatitude Pixelation (HEALPix) scheme.



**DEFINITION 3.1** [9]. A multifractional Gaussian process  $X(t)$ ,  $t \in [0, 1]$ , is a real Gaussian process whose covariance function  $C(t, s)$  is of the form

$$C(t, s) = \int_{\mathbb{R}} f(t, \lambda) \overline{f(s, \lambda)} d\lambda,$$

where

$$f(t, \lambda) = \frac{(e^{it\lambda} - 1)a(t, \lambda)}{|\lambda|^{1/2+\alpha(t)}}.$$

The smoothness of the process is determined by the function  $\alpha(\cdot)$  which is from  $C^1$  with  $0 < \alpha(t) < 1$ ,  $t \in [0, 1]$ . The modulation of the process is determined by the function  $a(t, \lambda)$  which is defined on  $[0, 1] \times \mathbb{R}$  and satisfies  $a(t, \lambda) = a_{\infty}(t) + R(t, \lambda)$ , where  $a_{\infty}(\cdot)$  is  $C^1([0, 1])$  with,  $a_{\infty}(t) \neq 0$  for all  $t \in [0, 1]$ , and  $R(\cdot, \cdot) \in C^{1,2}([0, 1] \times \mathbb{R})$  is such that there exists some  $\eta > 0$  that for  $i = 0, 1$  and  $j = 0, 2$  we have

$$\left| \frac{\partial^{i+j}}{\partial t^i \partial \lambda^j} R(t, \lambda) \right| \leq \frac{C}{|\lambda|^{\eta+j}}.$$

**DEFINITION 3.2** [38]. Multifractional Brownian motion (MBM) is given by

$$B_{H(t)}(t) = \frac{\sigma}{\Gamma(H(t) + 1/2)} \left\{ \int_{-\infty}^0 ((t-s)^{H(t)-1/2} - (-s)^{H(t)-1/2}) dB(s) + \int_0^t (t-s)^{H(t)-1/2} dB(s) \right\},$$

where  $B(s)$  is the standard Brownian motion and  $\sigma^2 = \text{Var}(B_{H(t)}(t))|_{t=1}$ .

For the MBM,  $E(B_{H(t)}(t)) = 0$  and  $\text{Var}(B_{H(t)}(t)) = \sigma^2 t^{2H(t)}/2$ . The FBM is a special case of the MBM where the local Hölder exponent  $H(t)$  is a constant, namely,  $H(t) = H$ . The MBM, which is a nonstationary Gaussian process, does not have independent stationary increments, in contrast to the FBM.

**DEFINITION 3.3.** A function  $H(\cdot) : \mathbb{R} \rightarrow \mathbb{R}$  is a  $(\beta, c)$ -Hölder function,  $\beta > 0$  and  $c > 0$ , if

$$|H(t_1) - H(t_2)| \leq c|t_1 - t_2|^{\beta}$$

for all  $t_1, t_2$  satisfying  $|t_1 - t_2| < 1$ .

The MBM admits the following harmonizable representation (see, for example, [10]). If  $H(\cdot) : \mathbb{R} \rightarrow [a, b] \subset (0, 1)$  is a  $\beta$ -Hölder function satisfying the assumption  $\sup H(t) < \beta$ , then the MBM with functional parameter  $H(\cdot)$  can be written as

$$\text{Re} \left( \int_{\mathbb{R}} \frac{(e^{it\xi} - 1)}{\|\xi\|^{H(t)+1/2}} d\tilde{W}(\xi) \right),$$



where  $\tilde{W}(\cdot)$  is the complex isotropic random measure that satisfies

$$d\tilde{W}(\cdot) = dW_1(\cdot) + idW_2(\cdot).$$

Here,  $W_1(\cdot)$  and  $W_2(\cdot)$  are independent real-valued Brownian measures.

We now introduce the concept of the *generalized multifractional Brownian motion* (GMBM), which is an extension of the FBM and MBM. The GMBM was introduced to overcome the limitations existed in applying the MBM to model data whose pointwise Hölder exponent has an irregular behaviour.

The following definitions will be used to analyse the CMB temperature intensities using the ring and nested ordering HEALPix schemes for  $d = 1, 2$ , respectively.

**DEFINITION 3.4 [7].** Let  $[a, b] \subset (0, 1)$  be an arbitrary fixed interval. An admissible sequence  $(H_n(\cdot))_{n \in \mathbb{N}}$  is a sequence of Lipschitz functions defined on  $[0, 1]$  and taking values in  $[a, b]$  with Lipschitz constants  $\delta_n$  such that  $\delta_n \leq c_1 2^{n\alpha}$ , for all  $n \in \mathbb{N}$ , where  $c_1 > 0$  and  $\alpha \in (0, a)$  are constants.

**DEFINITION 3.5 [7].** Let  $(H_n(\cdot))_{n \in \mathbb{N}}$  be an admissible sequence. The generalized multifractional field with the parameter sequence  $(H_n(\cdot))_{n \in \mathbb{N}}$  is the continuous Gaussian field  $Y(x, y)$ ,  $(x, y) \in [0, 1]^d \times [0, 1]^d$ , defined for all  $(x, y)$  as

$$Y(x, y) = \text{Re} \left( \int_{\mathbb{R}^d} \left( \sum_{n=0}^{\infty} \frac{(e^{ix\xi} - 1)}{\|\xi\|^{H_n(y)+1/2}} \hat{f}_{n-1}(\xi) \right) d\tilde{W}(\xi) \right),$$

where  $\tilde{W}(\cdot)$  is the stochastic measure defined previously.

The GMBM with the parameter sequence  $(H_n(\cdot))_{n \in \mathbb{N}}$  is the continuous Gaussian process  $X(t)$ ,  $t \in [0, 1]^d$  defined as the restriction of  $Y(x, y)$ ,  $(x, y) \in [0, 1]^d \times [0, 1]^d$  to the diagonal,  $X(t) = Y(t, t)$ .

Compared with the FBM and MBM, one of the major advantages of the GMBM is that its pointwise Hölder exponent can be defined through the parameter  $(H_n(\cdot))_{n \in \mathbb{N}}$ . For every  $t \in \mathbb{R}^2$ , almost surely,

$$\alpha_X(t) = H(t) = \liminf_{n \rightarrow \infty} H_n(t).$$

### 4. The Hölder exponent

This section presents basic notation, definitions and theorems associated with the pointwise Hölder exponent; see [7, 9, 24] for additional details. The pointwise Hölder exponent determines the regularity of a stochastic process. It describes local scaling properties of random fields, and can be used to detect multifractionality.

**DEFINITION 4.1 [7].** The pointwise Hölder exponent of a stochastic process  $X(t)$ ,  $t \in \mathbb{R}$ , whose trajectories are continuous, is the stochastic process  $\alpha_X(t)$ ,  $t \in \mathbb{R}$ , defined

for every  $t$  as

$$\alpha_X(t) = \sup \left\{ \alpha \mid \limsup_{h \rightarrow 0} \frac{|X(t+h) - X(t)|}{|h|^\alpha} = 0 \right\}.$$

The Hölder regularity of FBM can be specified at any given point  $t$ , almost surely, and  $\alpha_{B_H}(t) = H$  is constant for FBM. The pointwise Hölder regularity of MBM can be determined by its functional parameter similarly to FBM where  $\alpha_X(t)$  is the pointwise Hölder exponent. In particular, for every  $t \in \mathbb{R}$ , almost surely,  $\alpha_X(t) = H(t)$ .

In the literature, the method of quadratic variations is a frequently used technique to estimate the Hölder exponent [9, 24]. The following definition is used to compute the total increment in the one-dimensional case and will be applied for the ring ordering scheme of HEALPix points.

**DEFINITION 4.2** [7]. Let  $t \in [0, 1]$ . For every integer  $N \geq 2$ , the generalized quadratic variation  $V_N^{(1)}(t)$  around  $t$  is defined by

$$V_N^{(1)}(t) = \sum_{p \in v_N(t)} \left( \sum_{k \in F} e_k X\left(\frac{p+k}{N}\right) \right)^2, \tag{4.1}$$

where  $F = \{0, 1, 2\}$ ,  $e_0 = 1$ ,  $e_1 = -2$ ,  $e_2 = 1$ , and

$$v_N(t) = \{p \in \mathbb{N} \mid 0 \leq p \leq N - 2 \text{ and } |t - p/N| \leq N^{-\gamma}\}.$$

The following definition is used to compute the total increment in the two-dimensional case and will be used for the nested ordering scheme of HEALPix points.

**DEFINITION 4.3.** Let  $t = (t_1, t_2) \in [0, 1]^2$ . For every integer  $N \geq 2$ , the generalized quadratic variation  $V_N^{(2)}(t)$  around  $t$  is defined by

$$V_N^{(2)}(t) = \sum_{p \in v_N(t)} \left( \sum_{k \in F} d_k X\left(\frac{p+k}{N}\right) \right)^2, \tag{4.2}$$

where  $p = (p_1, p_2)$ ,  $\varepsilon = (\varepsilon_1, \varepsilon_2)$ ,  $(p + \varepsilon)/N = ((p_1 + \varepsilon_1)/N, (p_2 + \varepsilon_2)/N)$ ,  $F = \{0, 1, 2\}^2$  and, for all  $k = (k_1, k_2) \in F$ ,  $d_k = \prod_{l=1}^2 e_{k_l}$  with  $e_0 = 1$ ,  $e_1 = -2$  and  $e_2 = 1$ . Here,  $v_N(t) = v_N^1(t_1) \times v_N^2(t_2)$  and, for all  $i = 1, 2$ ,

$$v_N^i(t_i) = \{p_i \in \mathbb{N} \mid 0 \leq p_i \leq N - 2 \text{ and } |t_i - p_i/N| \leq N^{-\gamma}\}.$$

The pointwise Hölder exponents are estimated for the one-dimensional ring ordering and two-dimensional nested ordering of HEALPix points by considering sufficiently large  $N$  and  $d = 1, 2$ , respectively, in the following theorem which is a specialization of [7, Theorem 2.2] with  $\delta = 1$ .

**THEOREM 4.4** [7]. Let  $X(t)$ ,  $t \in [0, 1]^d$ , be a GMBM with an admissible sequence  $(H_n(\cdot))_{n \in \mathbb{N}}$  ranging in  $[a, b] \subset (0, 1 - 1/2d)$ . Then, for a fixed  $\gamma \in (b, 1 - 1/2d)$  and the

sequence  $(H_n(t))_{n \in \mathbb{N}}$  convergent to  $H(t)$ , we have

$$H(t) = \lim_{N \rightarrow \infty} \frac{1}{2} \left( d(1 - \gamma) - \frac{\log(V_N^{(d)}(t))}{\log(N)} \right) \quad (4.3)$$

almost surely.

## 5. Data and methodology

This section presents an overview of the data and key ideas of the suggested methodology to study multifractality of the CMB data that is based on theoretical results from Section 4. This and the next sections also provide a detailed justification of this methodology and its assumptions and required modifications of the formulas for the spherical case and CMB data.

In the cosmological literature, it is widely accepted that CMB data are a realization of random fields on a sphere. This paper follows this approach to study the local properties of the corresponding spherical random field. We have developed and implemented a method of computing local estimators in a neighbourhood of each pixel.

The CMB data are referenced by a very dense grid of pixels with equal areas on the sky sphere. They are stored according to the HEALPix format on the sphere. Each CMB pixel has a set of attributes, such as its unique location, temperature intensity and polarization data, which describe its properties. In this analysis the temperature intensities are used. The resolution parameter  $N_{\text{side}}$  defines the number of pixels  $N_{\text{pix}}$  on the sphere and their size. For example, for a given resolution  $N_{\text{side}} = 2048$ , there are  $N_{\text{pix}} = 12 \times (N_{\text{side}})^2 = 50\,331\,648$  pixels observed on the CMB sky sphere [18, 20, 22]. The CMB data are stored at 5 and 10 arc minutes resolution on the CMB sky for the resolution parameters  $N_{\text{side}} = 2048$  and  $N_{\text{side}} = 1024$ , respectively. To estimate local Hölder exponent values one needs a sufficient number of observations in a neighbourhood of a given point. The dense HEALPix grid provides such high-resolution data to reliably estimate local Hölder exponent values. For all numerical results and estimates, the highest available resolution  $N_{\text{side}} = 2048$  was used.

The Planck CMB intensity measurements vary in frequency from 30 to 857 GHz. They were obtained by separating the Planck CMB measurements from the foreground noise using several methods (COMMANDER, NILC, SEVEM and SMICA) [3]. In applied cosmological research, it's assumed that after separation, the residual foreground noise component of Planck CMB temperature intensities is negligible.

For multifractional data,  $H(t)$  changes from location to location and  $H(t) \neq \text{constant}$ , where  $t \in s_2(1)$ . Several methods to estimate the local Hölder exponent are available in the literature. Different methods often give different results regarding inconsistent estimation results of the Hölder exponent (see, for example, discussions in [11, 42]). Inconsistent results by different techniques are due to their different assumptions [11]. We propose an estimation method based on the generalized quadratic variations given by (4.1) and (4.2) and their asymptotic behaviour in (4.3). The results of this method

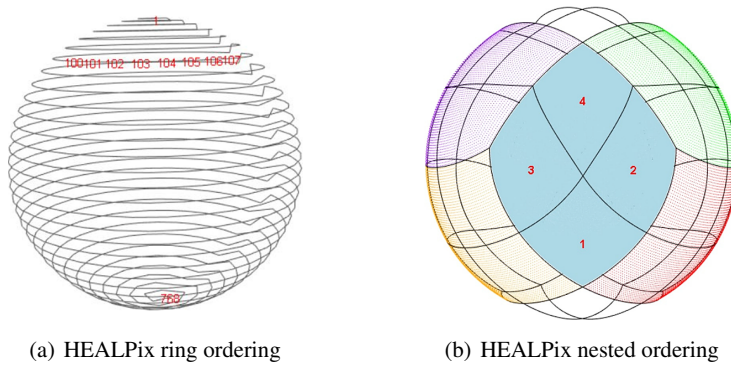


FIGURE 1. HEALPix ordering schemes.

are also compared with another conventional method that uses the rescale range (R/S) to estimate the Hölder exponent. This method is realized in the R package FRACTAL [17].

The CMB data exhibit variations of the temperature intensities at very small scales ( $\pm 1.8557 \times 10^{-3}$ ). To get reliable estimates of  $H(t)$ , a large number of observations in neighbourhoods of each  $t$  is required. Thus, in this paper, we do not discuss the preciseness of the local estimators of  $H(t)$ , but only pay attention to differences in the estimated values at different locations.

For computing purposes, the temperature intensities were scaled as

$$\text{scaled intensity}(t) = \frac{\text{intensity}(t)}{\max_{s \in S_2(1)} |\text{intensity}(s)|}.$$

It is clear from Definition 4.1 that this scaling does not change the values of  $\alpha_X(t)$ . Also, by (4.1) and (4.2) the generalized quadratic variation of the scaled process  $cX(t)$  is  $c^2 V_N^{(d)}(t)$ ,  $d = 1, 2$ . By (4.3),

$$\lim_{N \rightarrow \infty} \frac{\log(c^2 V_N^{(d)}(t))}{\log(N)} = \lim_{N \rightarrow \infty} \left( \frac{\log(c^2)}{\log(N)} + \frac{\log(V_N^{(d)}(t))}{\log(N)} \right) = \lim_{N \rightarrow \infty} \frac{\log(V_N^{(d)}(t))}{\log(N)}, \quad (5.1)$$

which means that this scaling also does not affect  $H(t)$ .

As mentioned before, for small values of  $\log(N)$  the estimates of  $H(t)$  can be biased, which is now evident from the term  $\log(c^2)/\log(N)$  in equation (5.1). However, this bias is due to the scaling effect only and is exactly the same for all values of  $t$ . Even if it might result in some errors in estimates  $\hat{H}(t)$ , it will not affect the analysis of differences in  $H(t)$  values for different locations, which is the main aim of this analysis.

Estimates of pointwise Hölder exponent values were computed using one- and two-dimensional regions of the CMB data and the HEALPix ring and nested orderings [20]. The ordering schemes are demonstrated in Figure 1. For fast computations we used the well-known advantages of these HEALPix ordering representations. The method of quadratic variation for Hölder exponents was adjusted for the nested

and ring representations on the sphere. Numerical studies showed that the proposed estimators are robust to changes of neighbourhood sizes.

## 6. Numerical studies

This section presents numerical studies and applications of the methodology from Section 5 to CMB data. The pointwise Hölder exponent estimates  $\hat{H}(t)$  are computed and analysed for one- and two-dimensional regions of the CMB temperature intensities acquired from the NASA/IPAC Infrared Science Archive [23]. The estimated Hölder exponents are used to quantify the roughness of the CMB temperature intensities. The methodology developed is also applied to detect possible anomalies in the CMB temperature intensities.

**6.1. Estimates of Hölder exponent for one-dimensional CMB regions** For the one-dimensional case, the HEALPix ring ordered CMB temperature intensities were modelled by a stochastic process  $X(t)$ . Their Hölder exponents  $H(t)$  were estimated by using the expression from equation (4.3) for the given large  $N$  with  $d = 1$ , where  $V_N^{(1)}(t)$  was computed using equation (4.1), which can be explicitly written as

$$V_N^{(1)}(t) = \sum_{p=0}^{N-2} \left( X\left(\frac{p}{N}\right) - 2X\left(\frac{p+1}{N}\right) + X\left(\frac{p+2}{N}\right) \right)^2.$$

As pixels on relatively small ring segments can be considered lying on approximately straight lines, the results from the case  $d = 1$  can be used. The parameter  $N$  was chosen to give approximately the number of pixels within a half ring of the CMB sky sphere. The parameter  $r$  is the distance from a HEALPix point  $t$  that is the centre of an interval in which we compute the total increment  $V_N^{(1)}(t)$ . By the expression for  $v_N(t)$  in Definition 4.2, the parameter  $\gamma$  was computed as  $\gamma = -(\log(r)/\log(N))$  for selected values of  $N$  and  $r$ . Then it was used in equation (4.3) to compute the estimated pointwise Hölder exponent values.

According to the HEALPix structure of the CMB data with resolution  $N_{\text{side}} = 2048$ , the HEALPix ring ordering scheme results in  $(4 \times N_{\text{side}} - 1)$  rings [22]. That is, for  $N_{\text{side}} = 2048$ , the CMB sky sphere consists of 8191 rings. Based on the HEALPix geometry, the number of pixels in the upper part rings increases with the ring number, Ring = 1, ..., 2047, as  $4 \times \text{Ring}$ . The  $(2N_{\text{side}} + 1) = 4097$  set of rings in the middle part of the CMB sky sphere have equal number of pixels,  $4 \times N_{\text{side}}$ . The number of pixels in each of the final  $(N_{\text{side}} - 1) = 2047$  rings in the lower part decreases according to the formula  $4 \times (8191 - \text{Ring} + 1)$ .

For the one-dimensional case, the estimated pointwise Hölder exponent values  $\hat{H}(t)$  were computed as follows. First, a random CMB pixel was selected and its ring was determined. Then pixels belonging to the half of that particular ring were selected. Then, for each CMB pixel in this rim segment, the quadratic variation was computed by  $V_N^{(1)}(t)$  given in equation (4.1). When computing the generalized quadratic variation for a CMB pixel, the pixels within a distance  $r = 0.08$  from it were considered. For

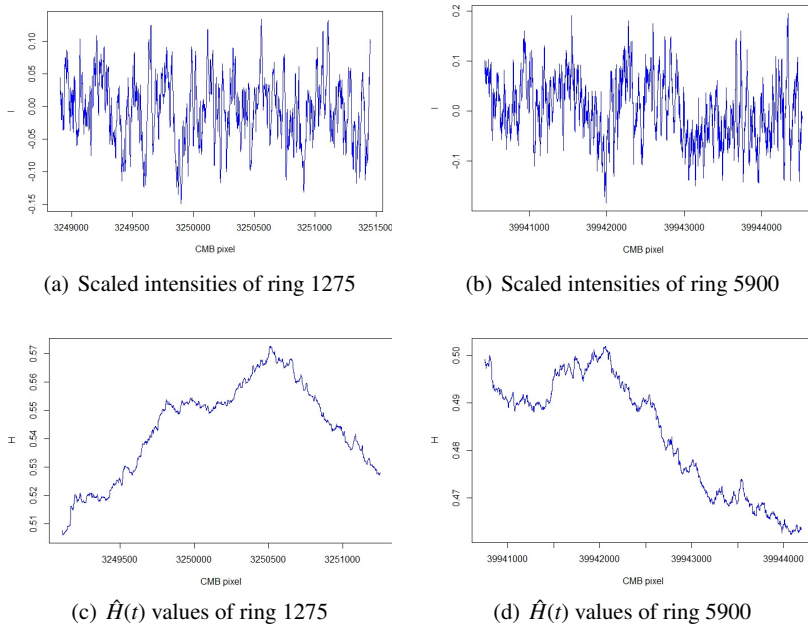


FIGURE 2. Examples of scaled intensities and  $\hat{H}(t)$  values for one-dimensional CMB regions.

these pixels, the squared increments were computed and used to obtain the total of increments. Finally, the Hölder exponents were estimated by substituting the total of increments and the other parameters in equation (4.3).

First, three CMB pixels “552300”, “1533000”, “3253800” located in the corresponding upper part rings 525, 875 and 1275 were chosen. Then for each CMB pixel in these half rings, their corresponding estimated Hölder exponents  $\hat{H}(t)$  were computed. Next, another three pixels “10047488”, “32575488”, “39948288” were chosen in the middle part of the CMB sky sphere. Their ring numbers were 2250, 5000 and 5900, respectively. Finally, three CMB pixels “47656664”, “48651704”, “49375304” belonging to the lower part rings, 7035, 7275 and 7500 were selected and the pointwise Hölder exponents of pixels in their rim segments were estimated.

For example, Figure 2 shows the plots of the scaled intensities and the estimated pointwise Hölder exponents of the rim segments of rings 1275 and 5900, which belong to the upper and middle parts of the CMB sky sphere, respectively. It can be seen from Figures 2(a) and 2(b) that the majority of scaled intensities fall into the range  $[-0.2, 0.2]$  and their fluctuations are random. Figures 2(c) and 2(d) show that the  $\hat{H}(t)$  values in both rim sections are changing and the dispersion range for ring 1275 is wider than that of ring 5900. Similar plots and results were also obtained for other rings.

The summary of the estimated pointwise Hölder exponent values obtained by the discussed methodology is shown in Table 1. It is clear that the dispersion range of the  $\hat{H}(t)$  values and the mean  $\hat{H}(t)$  value change with ring numbers. These results

TABLE 1. Summary of  $\hat{H}(t)$  values for pixels in different rings of the CMB sky sphere.

Part of CMB sky	Case	Ring number	$\gamma$	$[\hat{H}(t)_{\min}, \hat{H}(t)_{\max}]$	$\hat{H}(t)_{\max} - \hat{H}(t)_{\min}$	Mean $\hat{H}(t)$
Upper part	1	525	0.3631	[0.5681, 0.6215]	0.0534	0.5960
	2	875	0.3382	[0.5443, 0.5782]	0.0339	0.5605
	3	1275	0.3220	[0.5059, 0.5727]	0.0668	0.5439
Middle part	4	2250	0.3037	[0.4824, 0.5479]	0.0655	0.5137
	5	5000	0.3037	[0.4372, 0.4847]	0.0475	0.4626
	6	5900	0.3037	[0.4622, 0.5019]	0.0397	0.4835
Lower part	7	7035	0.3260	[0.5067, 0.5384]	0.0317	0.5234
	8	7275	0.3361	[0.5256, 0.5553]	0.0297	0.5410
	9	7500	0.3492	[0.5548, 0.5896]	0.0348	0.5701

TABLE 2. Summary of  $\hat{H}(t)$  values for pixels in different rings of the CMB sky sphere using the R/S method.

Part of CMB sky	Case	Ring number	$[\hat{H}(t)_{\min}, \hat{H}(t)_{\max}]$	$\hat{H}(t)_{\max} - \hat{H}(t)_{\min}$	Mean $\hat{H}(t)$
Upper part	1	525	[0.8106, 0.9035]	0.0929	0.8758
	2	875	[0.8527, 0.9146]	0.0619	0.8867
	3	1275	[0.8577, 0.9088]	0.0511	0.8898
Middle part	4	2250	[0.8757, 0.9148]	0.0391	0.8975
	5	5000	[0.8656, 0.9079]	0.0423	0.8883
	6	5900	[0.8702, 0.9072]	0.0370	0.8926
Lower part	7	7035	[0.8617, 0.9081]	0.0464	0.8889
	8	7275	[0.8599, 0.9098]	0.0499	0.8897
	9	7500	[0.8348, 0.9004]	0.0656	0.8714

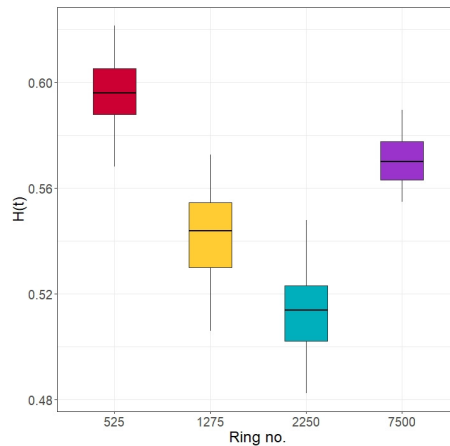
suggest that the pointwise Hölder exponent values change from location to location. The summary of the estimated pointwise Hölder exponent values obtained by the conventional (R/S) method using the command `RoverS` from the R package `FRACTAL` is given in Table 2. Note that the dispersion range and the mean  $\hat{H}(t)$  value change with the spiralling ring number. Similar results were also obtained for other available estimators of the Hölder exponent. Although these numerical values are inconsistent between different methods, they all suggest that the pointwise Hölder exponent values change from location to location.

It is expected that temperature intensities are positively dependent/correlated in close regions; see the covariance analysis in [13]. Therefore, running standard equality-of-means tests under independence assumptions will provide even more significant results if the hypothesis of equal means is rejected.



TABLE 3. The  $p$ -values for Wilcoxon tests between different rings.

1275	$3.048 \times 10^{-15}$		
2250	$7.939 \times 10^{-11}$	$3.606 \times 10^{-12}$	
7500	$1.533 \times 10^{-8}$	$4.605 \times 10^{-10}$	$3.717 \times 10^{-13}$
	525	1275	2250

FIGURE 3. The distribution of  $\hat{H}(t)$  values of four rim segments.

To prove that distributions of  $\hat{H}(t)$  are statistically different between different sky regions, we carried out several equality-of-means tests. Before that, the Shapiro test was used to ensure that the  $\hat{H}(t)$  values satisfy the normality assumption. For all the cases considered in Table 1, their  $\hat{H}(t)$  values failed the normality assumption. Since the CMB pixels close to each other can be dependent, to get more reliable results, we chose CMB pixels at distance 50 apart on a ring. The Shapiro test confirmed that in all the considered upper and lower part cases in Table 1,  $\hat{H}(t)$  values at step 50 satisfied the normality assumption, whereas the  $\hat{H}(t)$  values in the middle part failed the normality assumption.

Let  $\mu_1$  and  $\mu_2$  be the mean( $\hat{H}(t)$ ) values of the rim segments of rings 525 and 1275, respectively. To test the hypothesis  $H_0 : \mu_1 = \mu_2$  against  $H_1 : \mu_1 \neq \mu_2$ , we carried out the Wilcoxon test. The obtained  $p$ -value ( $3.048 \times 10^{-15}$ ) is significantly less than 0.05 and suggests that the means are different at the 5% level of significance. Similar results were obtained for the Wilcoxon tests between all pairs of the cases in Table 1. For example, Table 3 shows Wilcoxon test results for selected four rings, two in the upper part, and the other two correspondingly in the middle and lower parts of the CMB sky sphere. Figure 3 shows the distribution box plots of the  $\hat{H}(t)$  values in the rim segments of rings 525, 1275, 2250 and 7500. It is clear from Figure 3 that the mean( $\hat{H}(t)$ ) values are different from each other in these cases.

Analogously to Table 3, for all Wilcoxon tests between the rim sectors in the upper, middle and lower parts,  $p > 0.05$ . Therefore, there is enough statistical evidence to suggest that the pointwise Hölder exponents change from location to location. While we compared Hölder exponents for different rings, from Figure 2 it is clear that  $\hat{H}(t)$  is also changing for pixels within the same rings.

**6.2. Estimates of Hölder exponent for two-dimensional CMB regions** For two-dimensional sky regions, pointwise Hölder exponent values  $H(t)$  were estimated according to equation (4.3) with  $d = 2$ , where  $V_N^{(2)}(t)$  was computed using equation (4.2). Equation (4.2) in Definition 4.3 can be written in the following explicit form:

$$\begin{aligned} V_N^{(2)}(t) &= \sum_{p \in v_N(t)} \left\{ \sum_{k_1 \in \{0,1,2\}} \sum_{k_2 \in \{0,1,2\}} e_{k_1} e_{k_2} X\left(\frac{p_1 + k_1}{N}, \frac{p_2 + k_2}{N}\right) \right\}^2 \\ &= \sum_{p \in v_N(t)} \left\{ X\left(\frac{p_1}{N}, \frac{p_2}{N}\right) - 2X\left(\frac{p_1}{N}, \frac{p_2 + 1}{N}\right) - 2X\left(\frac{p_1 + 1}{N}, \frac{p_2}{N}\right) \right. \\ &\quad + X\left(\frac{p_1}{N}, \frac{p_2 + 2}{N}\right) + X\left(\frac{p_1 + 2}{N}, \frac{p_2}{N}\right) + 4X\left(\frac{p_1 + 1}{N}, \frac{p_2 + 1}{N}\right) \\ &\quad \left. - 2X\left(\frac{p_1 + 1}{N}, \frac{p_2 + 2}{N}\right) - 2X\left(\frac{p_1 + 2}{N}, \frac{p_2 + 1}{N}\right) + X\left(\frac{p_1 + 2}{N}, \frac{p_2 + 2}{N}\right) \right\}^2. \end{aligned}$$

To compute quadratic increments of spherical random fields, relatively small parts of the sphere can be approximately considered as regions of the plane and the above formula can be applied. Note that the internal summation set  $\{(p_1 + k_1)/N, (p_2 + k_2)/N \mid k_1, k_2 \in \{0, 1, 2\}\}$  can be very efficiently represented by the HEALPix nested structure. Indeed, all pixels have either seven or eight neighbours (see Figure 4). The  $3 \times 3$  configuration with eight neighbours perfectly matches the internal summation set and can be directly used in computations of  $V_N^{(2)}(t)$ . For the case of seven neighbours, an additional eighth neighbour, the intensity of which equals to that of its adjusted pixel, was imputed. For the resolution  $N_{\text{side}} = 2048$  only 24 out of 50 331 648 pixels have seven neighbours. For such a small number of pixels, the imputation has a negligible impact on the results.

Circular regions with radius  $R = 0.23$  were used in the computations in this section. Let  $N$  denote the number of pixels within such circular regions. Then,  $N \approx 662\,700$  pixels. To reduce the computation time, we chose a grid of 1000 CMB pixels with step  $662 = \lfloor 662\,700/1000 \rfloor$ , where  $\lfloor \cdot \rfloor$  denotes the integer part, over the total number of pixels. To compute local estimators  $\hat{H}(t)$ , for each chosen CMB pixel, a circular window with radius  $r = 0.01$  was selected. The value of  $\gamma$  was computed as  $\gamma = -(\log(\sqrt{\pi}r/2)/\log(\sqrt{N}))$  for given values of  $N$  and  $r$ . The factor  $\sqrt{\pi}/2$  appeared as the number of pixels is proportional to a window area. To match the number of pixels in circular window regions that were used in computations and square regions used for summation in  $V_N^{(2)}(t)$ , the length  $2d_0$  of the side of squares should satisfy the equation  $(2d_0)^2 = \pi r^2$ . The  $\gamma$  obtained was substituted in equation (4.3) to compute the estimated pointwise Hölder exponent values. For  $r = 0.01$ , there are approximately

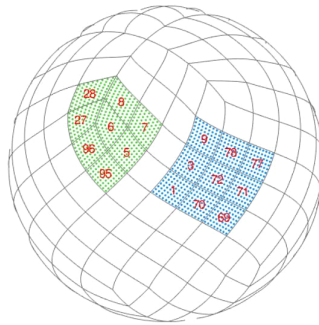


FIGURE 4. Examples of pixels with seven and eight neighbours for  $N_{\text{side}} = 4$ .

2836 pixels in each specified window. For each of these pixels, the squared increment was computed and the total of increments was obtained by the expression for  $V_N^{(2)}(t)$ .

Initially, the two-dimensional regions were selected randomly. Then, from those candidates, regions with majority warm, majority cold, a mixture of temperatures, and borderline regions were selected. The paper presents only results about those selected regions. Similar results were obtained for other analogous regions, but, due to space restrictions, are not given here.

First, a circular CMB sky window of radius  $R = 0.23$  from a warm area with a majority of high temperature intensities was selected. The mean temperature intensity in the selected CMB sky region covering the warm area was  $5.97861 \times 10^{-5}$ . The window is shown in Figure 5(a). The number of pixels in that specific window was 662 685. Then different circular CMB sky windows having a radius of  $R = 0.23$  covering cold, mixture, and borderline regions shown in Figures 5(b), 5(c) and 5(d) were chosen. In each of the cold, mixture of warm and cold and a borderline having warm and cold regions, the number of pixels were 662 697, 662 706 and 662 725, respectively. The value of  $\gamma$  was computed as  $\gamma = 0.705$  for each CMB sky region. The corresponding mean temperature intensities were  $-8.34055 \times 10^{-5}$ ,  $-1.74035 \times 10^{-5}$  and  $7.59851 \times 10^{-6}$ .

The plots of the estimated pointwise Hölder exponent values for each case are displayed in Figure 6. These  $\hat{H}(t)$  values are mostly dispersed in the interval  $[0.36, 0.86]$ . Figure 6 shows an erratic and an irregular behaviour in the distribution of  $\hat{H}(t)$  values. It can be observed that the estimates in Figures 6(a) and 6(d) with substantial warm temperatures have larger  $\hat{H}(t)$  fluctuations than the  $\hat{H}(t)$  values for cold regions.

The summary of the estimated pointwise Hölder exponents for each selected region is given in Table 4. It shows the mean CMB temperature intensities of each circular window. Table 4 also presents the estimated minimum, maximum and mean  $\hat{H}(t)$  values computed by using the selected 1000 CMB pixels. It is clear from this table that the mean  $\hat{H}(t)$  value from the warm region is the highest and it is the lowest for the borderline region. The mean  $\hat{H}(t)$  values of the cold region and mixture case lie in

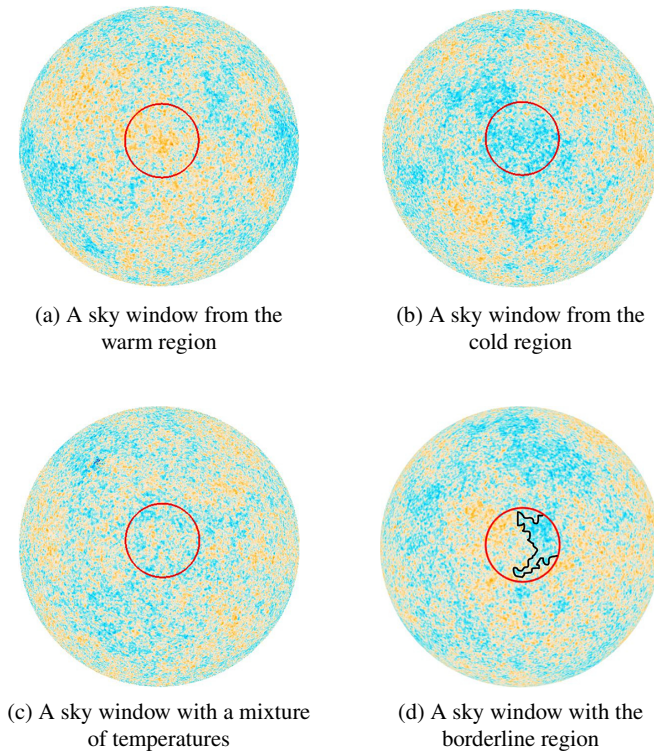


FIGURE 5. Sky windows used for computations.

between. It is apparent from Table 4 that the range of the estimated pointwise Hölder exponent values changes with respect to the temperature of the chosen regions of the CMB sky sphere.

To further investigate the estimated pointwise Hölder exponents, they were computed for 100 random CMB pixels in each of the regions considered. It was apparent that even if one accounts for variation by considering these 100 CMB pixels, the  $\hat{H}(t)$  values between different regions are different. The analyses suggested that all  $\hat{H}(t)$  values for 100 and 1000 CMB pixels were consistent. Therefore, the results suggest that the estimated pointwise Hölder exponent values change from place to place.

To prove that  $\hat{H}(t)$  is significantly different between different sky windows, we carried out several equality-of-means tests. Initially, we carried out the Shapiro test to ensure that the  $\hat{H}(t)$  values satisfy the normality assumption. However, for all the cases considered in Table 4, their  $\hat{H}(t)$  values failed the normality assumption. Figure 7 displays the distribution box plots of the  $\hat{H}(t)$  values in the CMB sky windows with warm, cold, mixture and borderline regions. It can be observed from Figure 7 that the  $\hat{H}(t)$  distributions have extreme values in all four cases. Thus, we present only results

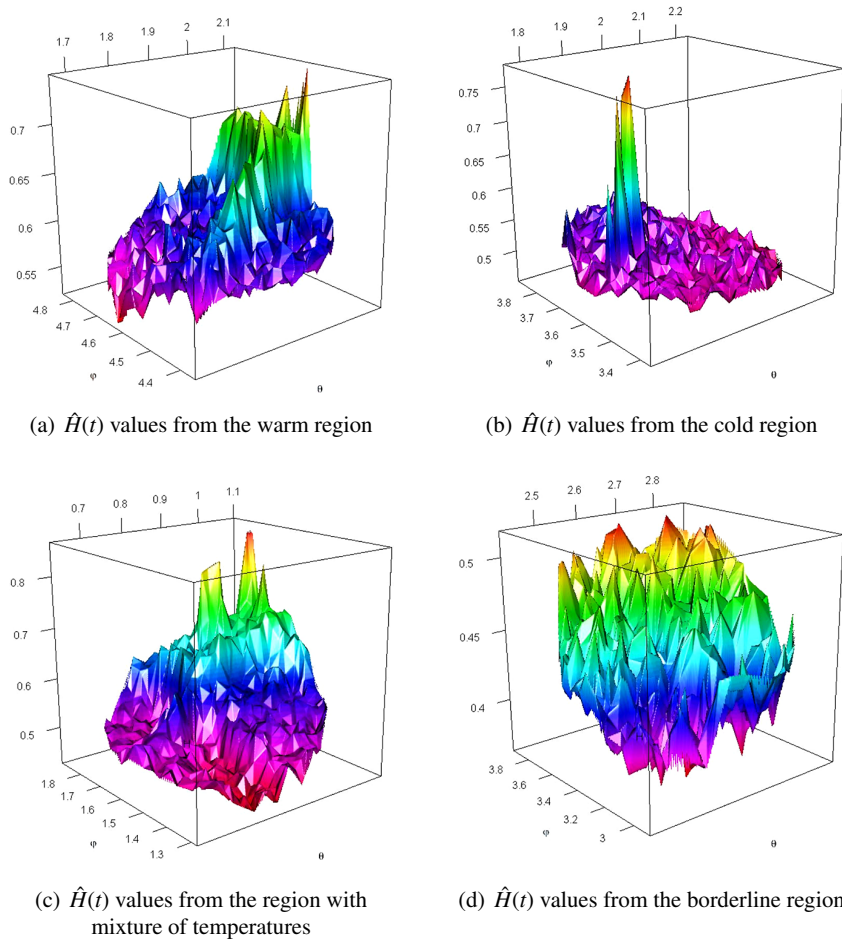


FIGURE 6. Local estimates  $\hat{H}(t)$  for two-dimensional regions.

from the Wilcoxon test as it is reliable amidst the nonnormality of data and in the presence of outliers.

Let  $\mu_1$  and  $\mu_2$  be the mean( $\hat{H}(t)$ ) values in the sky windows with warm and cold regions, respectively. Testing the hypothesis  $H_0 : \mu_1 = \mu_2$  against  $H_1 : \mu_1 \neq \mu_2$  using a Wilcoxon test, we obtained  $p < 2.2 \times 10^{-16}$ , highly significant at the 5% level. It suggests that the means are different at 5% level of significance. Similar results were obtained for the Wilcoxon tests between all pairs of the cases, and the corresponding  $p$ -values are shown in Table 5. This suggests that the mean( $\hat{H}(t)$ ) values are different from each other in all the cases. Apart from variations between the cases, we observe from Figure 6 and Table 4 that the estimated Hölder exponents do change within individual sky windows as well.

TABLE 4. Analysis of CMB sky windows with different temperatures.

Inspection Window	Mean Intensity	$[\hat{H}(t)_{\min}, \hat{H}(t)_{\max}]$	$\hat{H}(t)_{\min} - \hat{H}(t)_{\max}$	Mean $\hat{H}(t)$
Warm region	$5.978\ 6110^{-5}$	[0.5217, 0.7484]	0.2267	0.5994
Cold region	$-8.340\ 5510^{-5}$	[0.4534, 0.7806]	0.3272	0.5151
Mixture case	$-1.740\ 3510^{-5}$	[0.4302, 0.8592]	0.4290	0.5563
Borderline case	$7.598\ 5110^{-6}$	[0.3629, 0.5158]	0.1529	0.4407

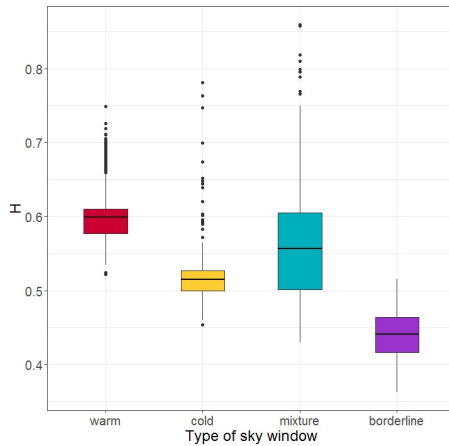


FIGURE 7. The distribution of  $\hat{H}(t)$  values for chosen sky windows.

TABLE 5. The  $p$ -values for Wilcoxon tests between chosen sky windows.

cold	$< 2.2 \times 10^{-16}$		
mixture	$< 2.2 \times 10^{-16}$	$< 2.2 \times 10^{-16}$	
borderline	$< 2.2 \times 10^{-16}$	$< 2.2 \times 10^{-16}$	$< 2.2 \times 10^{-16}$
	warm	cold	mixture

Therefore, there is enough evidence to suggest that the pointwise Hölder exponents change from location to location of the CMB sky sphere.

**6.3. Analysis of CMB temperature anomalies** As previously discussed in Section 1, several missions have measured the CMB temperature anisotropies, gradually increasing their precision by using advanced radio telescopes. This section discusses applications of the multifractional methodology to detect regions of CMB maps with “anomalies”. In particular, it can help in evaluating various reconstruction methods for blocked regions with unavailable or too noisy data.

It is well known that the CMB maps are affected by interference from the Milky Way, and radio signals emitting from our galaxy are much noisier than the CMB. Thus,



the Milky Way blocks the CMB near the galactic plane. However, the smooth and predictable nature of Milky Way's radiation spectrum has enabled the cosmological attributes to be found by subtracting the spectrum from the initially observed intensities [16]. From Planck 2015 results, the CMB maps have been cleaned and reconstructed using different techniques namely, COMMANDER, NILC, SEVEM and SMICA (see [3] for more information). We are using the CMB map produced from the SMICA method [23] with  $N_{\text{side}} = 2048$ .

To examine the random behaviour of isotropic Gaussian fields on the sphere, a direction-dependent mathematical tool has been proposed in [21]. The authors applied their probe to investigate the CMB maps from Planck PR2 2015 and PR3 2018 with specific consideration of cosmological data from the inpainted maps. To detect departures from the traditional stochastic model of the CMB data, they utilized the autocorrelation of the sequence of full-sky Fourier coefficients and have proposed an "AC discrepancy" function on the sphere. For the inpainted Planck 2015 COMMANDER map, [21] shows the maximum "AC discrepancy" for the galactic coordinates,  $(l, b) = (353.54, 1.79)$ . Similarly, for the inpainted Planck COMMANDER 2018, NILC 2018, SEVEM 2018 and SMICA 2018 with  $N_{\text{side}} = 1024$ , there are significant departures at the galactic coordinates  $(12.57, 0.11)$ ,  $(61.17, -30.73)$ ,  $(261.25, -2.99)$  and  $(261.34, -2.99)$ , respectively. A majority of these locations are the masked regions of the galactic plane. The galactic coordinates corresponding to the largest deviations are different for each map depicting the discrepancies in the underlying inpainting techniques.

The approach of Hamann et al. [21] used directional dependencies in CMB data on the unit sphere. The results below are based on a different approach that uses the local roughness properties of these data. Therefore, the detected regions of high anomalies can be different for these two methods as they reflect different physical anisotropic properties of CMB (see, for example, Figure 10). The estimated local Hölder exponents on one-dimensional rings can be considered as directional local probes of CMB anisotropy. However, the estimates for two-dimensional regions are more complex and aggregate local information about roughness in different directions.

In the following analysis, we use estimated values of the Hölder exponent to detect regions of possible anomalies in CMB maps. Figure 8 shows the plots of scaled intensities and estimated Hölder exponent values  $\hat{H}(t)$  in one- and two-dimensional CMB regions of the great circle. We notice from Figure 8(a) that there is an increase in the fluctuations of the scaled intensity values between the HEALPix range [25 163 000, 25 164 000] of the great circle ring. A low plateau of estimated  $\hat{H}(t)$  values in Figure 8(b) corresponds to that range of HEALPix values. The equator rim segment with the unusual plateau of  $\hat{H}(t)$  values has CMB pixel numbers ranging from 25 163 208 to 25 163 852. Their corresponding galactic coordinates were found to be between,  $(65.02, 0.01)$  and  $(93.32, 0.01)$ .

Similarly, this unusual behaviour of  $\hat{H}(t)$  values was observed in the two-dimensional CMB regions near the galactic plane/equator. Figure 8(c) shows the plot of scaled intensities in the two-dimensional space and a spike in intensities can be observed



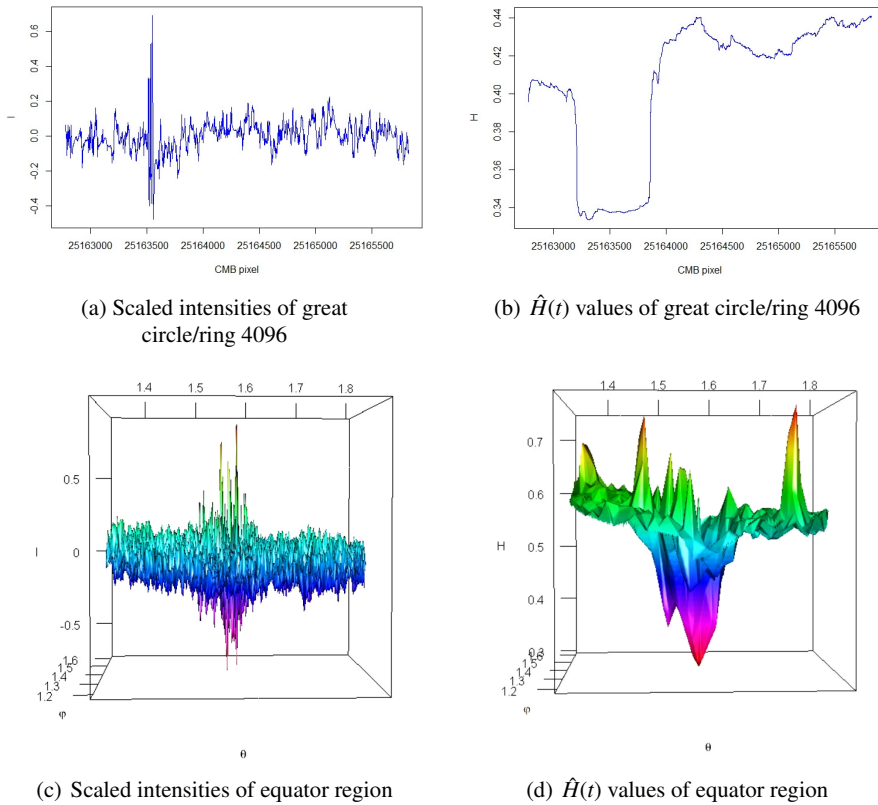


FIGURE 8. Scaled intensities and estimated  $\hat{H}(t)$  values in one- and two-dimensional regions of the great circle.

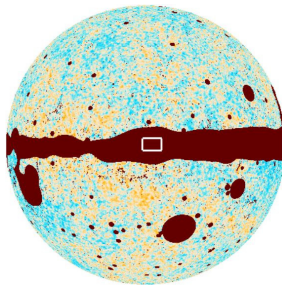
near the specified range of HEALPix values. The corresponding lower valley of  $\hat{H}(t)$  values can be seen in Figure 8(d). The four corners of the spherical region having unusual  $\hat{H}(t)$  values have HEALPix values 23 404 309, 23 391 936, 23 564 929 and 24 158 424. Their galactic coordinates were found as (85.91, -1.66), (76.82, -1.66), (76.82, 4.05) and (85.91, 4.05), respectively.

Table 6 shows the summary of CMB intensities at these one- and two-dimensional equatorial regions. The two-dimensional region around the unusual values was extracted as a rectangular spherical region from the circular CMB window using the previously identified galactic coordinates to split them as the unusual and the remaining regions. It is clear that the range of temperature intensities is wider in the one- and two-dimensional regions around the unusual values than in the regions excluding them. Further, the variances of intensities in the anomalous regions are larger than in the remaining regions. Moreover, Table 6 confirms that the mean  $\hat{H}(t)$  values in the anomalous regions are lower than in the remaining regions.

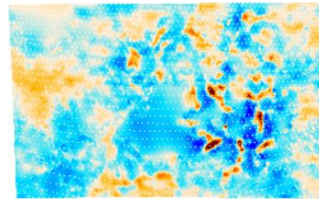
Figure 9 shows the Planck 2015 map with blocked nonreliable CMB values. The region of CMB values where the TMASK is applied by the SMICA reconstruction

TABLE 6. Analysis of CMB intensities near the equatorial region.

Inspection Window	$[I_{\min}, I_{\max}]$ (in $10^{-3}$ )	$I_{\max} - I_{\min}$ (in $10^{-3}$ )	Mean $I$ (in $10^{-5}$ )	Variance $I$ (in $10^{-8}$ )	$[\hat{H}(t)_{\min}, \hat{H}(t)_{\max}]$	$\hat{H}(t)_{\min}$ $-\hat{H}(t)_{\max}$	Mean $\hat{H}(t)$
One-dimensional region excluding the region of unusual values	$[-0.3688, 0.7578]$	1.1266	1.4846	1.5654	$[0.3351, 0.4411]$	0.1060	0.4168
One-dimensional region around unusual values	$[-0.8865, 1.2851]$	2.1716	-9.2156	4.9138	$[0.3336, 0.3496]$	0.0160	0.3384
Two-dimensional region excluding the region of unusual values	$[-0.3935, 0.2721]$	0.6656	-3.6390	1.1433	$[0.4097, 0.7448]$	0.3351	0.5489
Two-dimensional region around unusual values	$[-0.7310, 0.2751]$	1.0061	-6.3779	3.6978	$[0.3015, 0.5975]$	0.2960	0.4398



(a) The anomalous sky window



(b) The enlarged anomalous sky window

FIGURE 9. SMICA 2015 map with TMAPSK and the region of anomalies.

technique, is removed in Figure 9. The TMAPSK of the CMB intensities utilized by the SMICA method determines the region where the inpainted CMB intensities in the galactic plane are considered to be reliable. The rectangular window shows a possible region of anomalies detected by the developed multifractal methodology.

We now apply this approach and investigate  $\hat{H}(t)$  for all  $t \in s_2(1)$ . First, the one-dimensional methodology was used.  $\hat{H}(t)$  was estimated using the CMB intensities on rims, similar to the analysis in Figures 8(a) and 8(b). The moving windows with 4096 consecutive pixels, which is approximately half of a full ring, were used to obtain values of  $\hat{H}(t)$ . To clearly show local behaviours, after several trials, sets  $v_N(t)$  with 61 HEALPix points, that is, where the radius equals 30 pixels, were selected. The results obtained are shown in Figure 10(a). To compare them with the AC discrepancy approach in [21], Figure 10(b) shows the corresponding map obtained by applying the direction-dependent probe. The code from [44] was used to compute values of AC

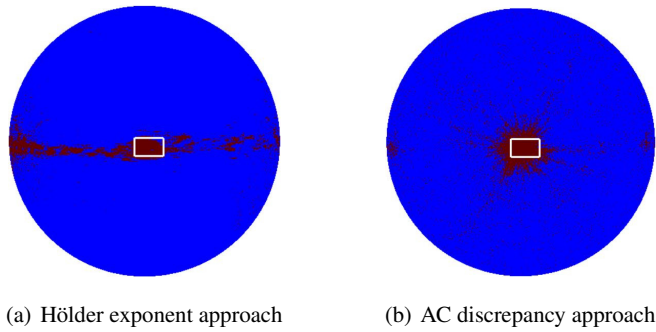


FIGURE 10. Discrepancy maps for CMB intensities from SMICA 2015.

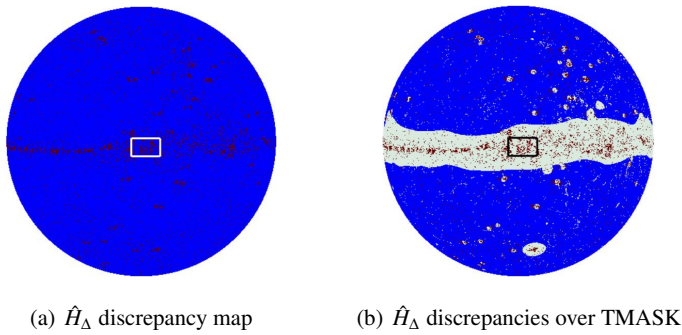


FIGURE 11.  $\hat{H}_\Delta$  discrepancy maps for CMB intensities from SMICA 2015.

discrepancies for SMICA 2015 CMB intensities. The first map highlights  $\hat{H}(t)$  values below the 5th percentile. AC discrepancy values above the 95th percentile were used for the second map. Both approaches detected the region of anomalies in Figure 9. However, from locations of other discrepancy values, it is clear that these approaches detect different CMB anomalies.

Very sharp changes in  $\hat{H}(t)$  values in Figure 8(b) motivated the second method to detect anomalies, which is based on increments of  $\hat{H}(t)$  values. Figure 8(b) demonstrated substantial changes of  $\hat{H}(t)$  for nearby  $t$  locations. These changes are permanent as  $\hat{H}(t)$  exhibits stable behaviour after a rapid “jump”. Such changes are different from noise or outliers, when values in random distinct locations lie at an abnormal distance from other values in their surrounding points.

To detect such rapid changes, we used the statistics  $\hat{H}_\Delta(t) = \min_{t_1 \in \Delta(t)} |\hat{H}(t) - \hat{H}(t_1)|$ , where  $t$  and  $t_1$  are indices of ring-ordered pixels and the set  $\Delta(t) = \{t + 10, \dots, t + 20\}$ . The delay of 10 was selected to detect jumps that occur over short distances. The minimum over the set of consecutive points  $\Delta(t)$  was used to eliminate outliers or noise that can result in distinct large differences  $|\hat{H}(t) - \hat{H}(t_1)|$ .

Figure 11(a) shows the computed  $\hat{H}_\Delta(t)$  values for SMICA 2015 CMB intensities. Here,  $\hat{H}_\Delta(t)$  values above the 95th percentile are plotted.

It is well known that the galactic centre and equatorial region are the most problematic and questionable areas of the CMB maps. Our methodology classified the galactic centre as anomalous based on its Hölder exponent value above the 95th percentile. The contextualization has been already provided by Hamann et al. [21]; it is due to difficulties in producing correct cleaned CMB maps in this region.

In Figure 11(b), 5% of largest  $\hat{H}_\Delta(t)$  values are shown on the TMAPSK map. Note that in most cases, clusters of largest  $\hat{H}_\Delta(t)$  values are within the TMAPSK. It seems that  $\hat{H}_\Delta$  indices rather accurately detected many regions with unreliable CMB values. Analysis of other CMB maps gave similar results.

Summarizing, the methodology implemented to investigate multifractional presence within the CMB temperature intensities could also serve as a mechanism to detect regions of anomalies in CMB maps.

## 7. Conclusion

In this paper, we examined multifractional spherical random fields and their application to analysis of cosmological data from the Planck mission. The paper developed the general methodology for estimation of pointwise Hölder exponents of multifractional data observed on the unit sphere. It estimated pointwise Hölder exponent values for the actual CMB temperature intensities and checked for the presence of multifractionality. The estimators of pointwise Hölder exponents for one- and two-dimensional regions were obtained by using the ring and nested orderings of the HEALPix visualization structure. The analysis carried out conveyed multifractionality in the CMB temperature intensities, since the computed pointwise Hölder exponent values do substantially change from place to place in the CMB sky sphere. The proposed method was used for numerical studies of the CMB data and found anisotropies in the temperature intensities. In particular, validity and usefulness of the method were evidenced by detecting numerous anisotropies in unreliable CMB regions of the TMAPSK.

The approach developed and the computing techniques implemented can also be used for other types of spherical data, such as solar data, planetary data, meteorological data, pollution data and earth data. First, the R package RCOSMO [18] can be used to transform spherical data into the HEALPix format. Then the methods developed can be directly applied by using the publicly available R code for this paper.

Some numerical approaches that were used to speed up computations for big CMB data sets will be reported in future publications. In future studies, it would be also interesting to:

- develop the distribution theory for the estimators of  $H(t)$ ;
- investigate reliability and accuracy of various estimators of the Hölder exponent for the CMB;
- study rates of convergence in Theorem 4.4 (see results on superconvergence by McLean [35]);

- investigate changes of the Hölder exponents depending on evolutions of random fields driven by SPDEs on the sphere [5, 13, 14];
- study directional changes of the Hölder exponent by extending the results obtained for the conventional ring ordering to rings with arbitrary orientations;
- apply our methodology to other spherical data, in particular, to new high-resolution CMB data from future CMB-S4 surveys [1];
- explore relations between the locations of the detected CMB anomalies and other cosmic objects.

At high values of  $l$ , the signal will be weakened by Silk damping and possibly clouded by pressure variations due to turbulence within the plasma, as currently observed in stars. We feel that it is worthwhile to analyse the full signal that is currently available. Higher-resolution measurements in the future will distinguish how much of the analysis is due to physical causes or currently remaining galactic noise.

### Acknowledgements

This research was partially supported under the Australian Research Council's Discovery Projects funding scheme (project no. DP160101366). We would like to thank Prof. A. Ayache for attracting our attention to and discussing multifractional models for random fields and Prof. I. Sloan for various discussions about mathematical modelling of CMB data. The authors are also grateful to the referees for their suggestions that helped to improve the style of the paper.

This research includes computations using the Linux computational cluster Gadi of the National Computational Infrastructure (NCI), which is supported by the Australian Government and La Trobe University. We are also grateful for the use of data on the Planck/ESA mission from the Planck Legacy Archive.

### References

- [1] K. Abazajian et al., "CMB-S4 science case, reference design, and project plan", Preprint, 2019, [arXiv:1907.04473](https://arxiv.org/abs/1907.04473).
- [2] S. Adachi et al., "A measurement of the CMB E-mode angular power spectrum at subdegree scales from 670 square degrees of POLARBEAR data", *Astrophys. J.* **904** (2020) Article ID 65; doi:[10.3847/1538-4357/abbacd](https://doi.org/10.3847/1538-4357/abbacd).
- [3] P. A. R. Ade et al., "Planck 2015 results-XVI. Isotropy and statistics of the CMB", *Astron. Astrophys.* **594** (2016) 1–62; doi:[10.1051/0004-6361/201526681](https://doi.org/10.1051/0004-6361/201526681).
- [4] N. Aghanim et al., "Planck 2018 results-VI. Cosmological parameters", *Astron. Astrophys.* **641** (2020) 1–67; doi:[10.1051/0004-6361/201833910](https://doi.org/10.1051/0004-6361/201833910).
- [5] V. Anh, P. Broadbridge, A. Olenko and Y. G. Wang, "On approximation for fractional stochastic partial differential equations on the sphere", *Stoch. Environ. Res. Risk Assess.* **32** (2018) 2585–2603; doi:[10.1007/s00477-018-1517-1](https://doi.org/10.1007/s00477-018-1517-1).
- [6] A. Ayache, *Multifractional stochastic fields: wavelet strategies in multifractional frameworks* (World Scientific, Singapore, 2018). doi:[10.1142/8917](https://doi.org/10.1142/8917).
- [7] A. Ayache and J. Véhel, "On the identification of the pointwise Hölder exponent of the generalized multifractional Brownian motion", *Stoch. Process. Appl.* **111** (2004) 119–156; doi:[10.1016/j.spa.2003.11.002](https://doi.org/10.1016/j.spa.2003.11.002).

- [8] M. Baiesi, C. Burigana, L. Conti, G. Falasco, C. Maes, L. Rondoni and T. Trombetti, “Possible nonequilibrium imprint in the cosmic background at low frequencies”, *Phys. Rev. Res.* **2** (2020) Article ID 013210; doi:[10.1103/PhysRevResearch.2.013210](https://doi.org/10.1103/PhysRevResearch.2.013210).
- [9] A. Benassi, S. Cohen and J. Istas, “Identifying the multifractional function of a Gaussian process”, *Statist. Probab. Lett.* **39** (1998) 337–345; doi:[10.1016/S0167-7152\(98\)00078-9](https://doi.org/10.1016/S0167-7152(98)00078-9).
- [10] A. Benassi, D. Roux and S. Jaffard, “Elliptic Gaussian random processes”, *Rev. Mat. Iberoam.* **13** (1997) 19–90; doi:[10.4171/rmi/217](https://doi.org/10.4171/rmi/217).
- [11] S. Bianchi, “Pathwise identification of the memory function of multifractional Brownian motion with application to finance”, *Int. J. Theor. Appl. Finance* **8** (2005) 255–281; doi:[10.1142/S0219024905002937](https://doi.org/10.1142/S0219024905002937).
- [12] P. Broadbridge and K. Deutscher, “Solution of non-autonomous Schrödinger equation for quantized de Sitter Klein-Gordon oscillator modes undergoing attraction-repulsion transition”, *Symmetry* **12** (2020) Article ID 943; doi:[10.3390/sym12060943](https://doi.org/10.3390/sym12060943).
- [13] P. Broadbridge, A. Kolesnik, N. Leonenko and A. Olenko, “Random spherical hyperbolic diffusion”, *J. Stat. Phys.* **177** (2019) 889–916; doi:[10.1007/s10955-019-02395-0](https://doi.org/10.1007/s10955-019-02395-0).
- [14] P. Broadbridge, A. Kolesnik, N. Leonenko, A. Olenko and D. Omari, “Spherically restricted random hyperbolic diffusion”, *Entropy* **22** (2020) Article ID 217; doi:[10.3390/e22020217](https://doi.org/10.3390/e22020217).
- [15] G. Calcagni, S. Kuroyanagi and S. Tsujikawa, “Cosmic microwave background and inflation in multifractional spacetimes”, *J. Cosmol. Astropart. Phys.* **8** (2016) Article ID 039; doi:[10.1088/1475-7516/2016/08/039](https://doi.org/10.1088/1475-7516/2016/08/039).
- [16] D. Castelvechi, “The quest to unlock the secrets of the baby universe”, *Nature* **572** (2019) 298–302; doi:[10.1038/d41586-019-02417-7](https://doi.org/10.1038/d41586-019-02417-7).
- [17] W. Constantine and D. Percival, “Fractal: a fractal time series modeling and analysis package”, *R package version 2.0-4* (2017), Retrieved from <https://CRAN.R-project.org/package=fractal>.
- [18] D. Fryer, M. Li and A. Olenko, “rcosmo: R package for analysis of spherical, HEALPix and cosmological data”, *R J.* **12** (2020) 206–225; <https://journal.r-project.org/archive/2020/RJ-2020-012/RJ-2020-012.pdf>.
- [19] D. Fryer, A. Olenko, M. Li and Y. G. Wang, “rcosmo: Cosmic microwave background data analysis”, *R package version 1.1.0* (2019) Retrieved from <https://CRAN.R-project.org/package=rcosmo>.
- [20] K. M. Gorski, E. Hivon, A. Banday, B. D. Wandelt, F. K. Hansen, M. Reinecke and M. Bartelmann, “HEALPix: a framework for high-resolution discretization and fast analysis of data distributed on the sphere”, *Astrophys. J.* **622** (2005) 759–771; doi:[10.1086/427976](https://doi.org/10.1086/427976).
- [21] J. Hamann, Q. T. L. Gia, I. H. Sloan, Y. G. Wang and R. S. Womersley, “A new probe of Gaussianity and isotropy with application to cosmic microwave background maps”, *Internat. J. Modern Phys. C* **32** (2021) Article ID 2150084; doi:[10.1142/S0129183121500844](https://doi.org/10.1142/S0129183121500844).
- [22] E. Hivon, “Geometric and algebraic properties of HEALPix” (2022), <https://healpix.jpl.nasa.gov/html/intrnode4.htm> (Accessed 20 June 2022).
- [23] IRSA, “NASA/IPAC infrared science archive”, <https://irsa.ipac.caltech.edu/data/Planck/release-2/all-sky-maps/maps/component-maps/cmb/> (Accessed 20 June 2022).
- [24] J. Istas and G. Lang, “Quadratic variations and estimation of the local Hölder index of a Gaussian process”, *Ann. Inst. H. Poincaré Probab. Statist.* **33** (1997) 407–436; doi:[10.1016/S0246-0203\(97\)80099-4](https://doi.org/10.1016/S0246-0203(97)80099-4).
- [25] R. Khatri and R. A. Sunyaev, “Creation of the CMB spectrum: precise analytic solutions for the blackbody photosphere”, *J. Cosmol. Astropart. Phys.* **2012** (2012) Article ID 038; doi:[10.1088/1475-7516/2012/06/038](https://doi.org/10.1088/1475-7516/2012/06/038).
- [26] Y. L. Klimontovich, *The statistical theory of non-equilibrium processes in a plasma* (Pergamon Press, Oxford, 1967).
- [27] A. Lang and C. Schwab, “Isotropic Gaussian random fields on the sphere: regularity, fast simulation and stochastic partial differential equations”, *Ann. Appl. Probab.* **25** (2015) 3047–3094; doi:[10.1214/14-AAP1067](https://doi.org/10.1214/14-AAP1067).



- [28] Q. T. Le Gia and J. Peach, “A spectral method to the stochastic Stokes equations on the sphere”, *ANZIAM J.* **60** (2019) C52–C64; doi:[10.21914/anziamj.v60i0.13987](https://doi.org/10.21914/anziamj.v60i0.13987).
- [29] N. Leonenko, R. Nanayakkara and A. Olenko, “Analysis of spherical monofractal and multifractal random fields”, *Stoch. Environ. Res. Risk Assess.* **35** (2021) 681–701; doi:[10.1007/s00477-020-01911-z](https://doi.org/10.1007/s00477-020-01911-z).
- [30] A. Malyarenko, *Invariant random fields on spaces with a group action* (Springer, Berlin, 2012), doi:[10.1007/978-3-642-33406-1](https://doi.org/10.1007/978-3-642-33406-1).
- [31] B. B. Mandelbrot and J. W. Van Ness, “Fractional Brownian motions, fractional noises and applications”, *SIAM Rev.* **10** (1968) 422–437; doi:[10.1137/1010093](https://doi.org/10.1137/1010093).
- [32] D. Marinucci, “Testing for non-Gaussianity on cosmic microwave background radiation: a review”, *Statist. Sci.* **19** (2004) 294–307; doi:[10.1214/088342304000000783](https://doi.org/10.1214/088342304000000783).
- [33] D. Marinucci and G. Peccati, *Random fields on the sphere: representation, limit theorems and cosmological applications* (Cambridge University Press, New York, 2011); doi:[10.1017/CBO9780511751677](https://doi.org/10.1017/CBO9780511751677).
- [34] A. C. Mathias, R. L. Viana, T. Kroetz and I. L. Caldas, “Fractal structures in the chaotic motion of charged particles in a magnetized plasma under the influence of drift waves”, *Phys. A* **469** (2017) 681–694; doi:[10.1016/j.physa.2016.11.049](https://doi.org/10.1016/j.physa.2016.11.049).
- [35] W. McLean, “Implementation of high-order, discontinuous Galerkin time stepping for fractional diffusion problems”, *ANZIAM J.* **62** (2020) 121–147; doi:[10.1017/S1446181120000152](https://doi.org/10.1017/S1446181120000152).
- [36] M. Minkov, M. Pinkwart and P. Schupp, “Entropy methods for CMB analysis of anisotropy and non-Gaussianity”, *Phys. Rev. D* **99** (2019) Article ID 103501; doi:[10.1103/PhysRevD.99.103501](https://doi.org/10.1103/PhysRevD.99.103501).
- [37] NASA, “Tests of big bang: the CMB”, [https://wmap.gsfc.nasa.gov/universe/bb\\_tests\\_cmb.html](https://wmap.gsfc.nasa.gov/universe/bb_tests_cmb.html) (Accessed 20 June 2022).
- [38] R. Péltier and J. Véhel, “Multifractal Brownian motion: definition and preliminary results”, Technical Report, 2645, Institut National de Recherche en Informatique et en Automatique, Le Chesnay Cedex, France, 1995, <https://hal.inria.fr/inria-00074045>.
- [39] Planck Science Team, *Planck*, <https://www.cosmos.esa.int/web/planck> (Accessed 20 June 2022).
- [40] A. G. Riess, S. Casertano, W. Yuan, L. M. Macri and D. Scolnic, “Large Magellanic Cloud Cepheid standards provide a 1% foundation for the determination of the Hubble constant and stronger evidence for physics beyond  $\lambda$  CDM”, *Astrophys. J.* **876** (2019) Article ID 85; doi:[10.3847/1538-4357/ab1422](https://doi.org/10.3847/1538-4357/ab1422).
- [41] H. Sheng, Y. Chen and T. Qiu, *Fractional processes and fractional-order signal processing: techniques and applications* (Springer, London, 2011). doi:[10.1007/978-1-4471-2233-3](https://doi.org/10.1007/978-1-4471-2233-3).
- [42] Z. Struzik, “Determining local singularity strengths and their spectra with the wavelet transform”, *Fractals* **8** (2000) 163–179; doi:[10.1142/S0218348X00000184](https://doi.org/10.1142/S0218348X00000184).
- [43] R. L. Viana, E. C. Da Silva, T. Kroetz, I. L. Caldas, M. Roberto and M. A. F. Sanjuán, “Fractal structures in nonlinear plasma physics”, *Philos. Trans. Roy. Soc. A* **369** (2011) 371–395; doi:[10.1098/rsta.2010.0253](https://doi.org/10.1098/rsta.2010.0253).
- [44] Y. G. Wang, “CMBProbe, the Python package for generating AC discrepancy maps” (2022), <https://github.com/wangyg19/CMBProbe> (Accessed 20 June 2022).
- [45] S. Weinberg, *Cosmology* (Oxford University Press, Oxford, 2008).